OBSERVATION OF A MORETON WAVE AND WAVE–FILAMENT INTERACTIONS ASSOCIATED WITH THE RENOWNED X9 FLARE ON 1990 MAY 24

Rui Liu[1], Chang Liu[2], Yan Xu[2], Wei Liu[3,4], Bernhard Kliem[5,6,7], and Haimin Wang[2]

[1] CAS Key Laboratory of Geospace Environment, Department of Geophysics and Planetary Sciences,
University of Science and Technology of China, Hefei 230026, China; rliu@ustc.edu.cn
[2] Space Weather Research Laboratory, Center for Solar-Terrestrial Research, NJIT, Newark, NJ 07102, USA
[3] Lockheed Martin Solar and Astrophysics Laboratory, Building 252, 3251 Hanover Street, Palo Alto, CA 94304, USA
[4] W. W. Hansen Experimental Physics Laboratory, Stanford University, Stanford, CA 94305, USA
[5] Institute of Physics and Astronomy, University of Potsdam, D-14476 Potsdam, Germany
[6] Mullard Space Science Laboratory, University College London, Holmbury St. Mary, Dorking, Surrey RH5 6NT, UK
[7] Yunnan Astronomical Observatory, Chinese Academy of Sciences, Kunming 650011, China

ABSTRACT

Using Big Bear Solar Observatory film data recently digitized at NJIT, we investigate a Moreton wave associated with an X9 flare on 1990 May 24, as well as its interactions with four filaments F1–F4 located close to the flaring region. The interaction yields interesting insight into physical properties of both the wave and the filaments. The first clear Moreton wavefront appears at the flaring-region periphery at approximately the same time as the peak of a microwave burst and the first of two γ-ray peaks. The wavefront propagates at different speeds ranging from 1500–2600 km s^{-1} in different directions, reaching as far as 600 Mm away from the flaring site. Sequential chromospheric brightenings are observed ahead of the Moreton wavefront. A slower diffuse front at 300–600 km s^{-1} is observed to trail the fast Moreton wavefront about one minute after the onset. The Moreton wave decelerates to ~550 km s^{-1} as it sweeps through F1. The wave passage results in F1's oscillation which is featured by ~1 mHz signals with coherent Fourier phases over the filament, the activation of F3 and F4 followed by gradual recovery, but no disturbance in F2. Different height and magnetic environment together may account for the distinct responses of the filaments to the wave passage. The wavefront bulges at F4, whose spine is oriented perpendicular to the upcoming wavefront. The deformation of the wavefront is suggested to be due to both the forward inclination of the wavefront and the enhancement of the local Alfvén speed within the filament channel.

Key words: Sun: filaments, prominences – Sun: flares – Sun: oscillations – waves

Online-only material: animations, color figures

1. INTRODUCTION

Recent observations of various large-scale waves and shocks in the solar corona (see the review by Warmuth 2007) have reignited interest in Moreton waves, which have been known for several decades (Moreton & Ramsey 1960; Moreton 1960). Moreton waves are flare-associated transients rapidly propagating across the solar surface in chromospheric spectral lines (typically in Hα and He i 10803 Å), whose speeds range from ~550 to ~2500 km s^{-1} (Moreton 1960; Athay & Moreton 1961; Smith & Harvey 1971; Warmuth et al. 2001, 2004a; Temmer et al. 2009; Balasubramaniam et al. 2010; Muhr et al. 2010). At some distance ($\simeq$100 Mm) from the flare site, they often appear as arc-shaped fronts (with an angular width of $\simeq$100°) propagating away from the flaring active region that last for only minutes and soon become irregular and diffuse. In the remote region, they often cause the activation or "winking" of filaments, i.e., a fading or disappearance followed by re-appearance of the filaments in the Hα line center (Ramsey & Smith 1966). The wavefronts appear bright in the Hα center and blue wing, while they appear dark in the red wing, which is interpreted as a depression of the chromosphere. Accordingly, a "winking" filament shifts from the Hα center to the red wing and then the blue wing (Dodson & Hedeman 1964). Uchida (1968) developed a theory interpreting Moreton waves as the "hemline" of a coronal fast-mode MHD wavefront sweeping over the chromosphere. The enhanced pressure behind the wavefront compresses the chromospheric plasma, which is observed as the down-up swing in

Hα filtergrams, and recently detected as EUV redshifts (Harra et al. 2011; Veronig et al. 2011) or seen in EUV images (Liu et al. 2012b). As the Alfvén speed increases with height in the low corona, it is expected that the wavefront of a coronal fast-mode MHD wave is forwardly inclined toward the solar surface, which is observed in some limb events (e.g., Hudson et al. 2003; Liu et al. 2012b) and reproduced by numerical simulations (e.g., Wu et al. 2001; Grechnev et al. 2011). In a recent observation, an Hα Moreton wavefront is observed to be the ground track of a dome-shaped coronal shock front (Asai et al. 2012; Shen & Liu 2012). Although Uchida's theory is generally accepted, the search for the coronal counterpart of Moreton waves is not free of controversies (e.g., Chen et al. 2005; Wills-Davey & Attrill 2009). It is also under debate whether Moreton waves are freely propagating or driven by coronal mass ejections (CMEs) acting as a piston.

Filament oscillations triggered by Moreton or coronal waves are often of large amplitude (>20 km s^{-1}; see the review by Tripathi et al. 2009), distinct from commonly observed small-amplitude oscillations (~2–3 km s^{-1}; see the review by Arregui et al. 2012), which are usually local and seemingly intrinsic to the filament itself without any obvious trigger. The physical nature of the wave–filament interaction is not well understood as observations are relatively scarce (Ramsey & Smith 1966; Hyder 1966; Eto et al. 2002; Okamoto et al. 2004; Gilbert et al. 2008; Hershaw et al. 2011; Liu et al. 2012b; Jackiewicz & Balasubramaniam 2013), and a filament does not always oscillate when a wave passes by (Okamoto et al. 2004). Ramsey

& Smith (1966) and Hyder (1966) studied 11 winking filaments and derived oscillatory periods between 6 and 40 minutes, and damping times between 7 and 120 minutes. They suggested that each filament has its own characteristic frequency of oscillation, noting that a filament perturbed by waves from four flares during three consecutive days oscillated with essentially the same frequency and damping time. They also reported a lack of correlation between the frequency and the filament dimensions, the distance to the perturbing flare or its size.

In most of the wave–filament interactions, the material undergoes vertical oscillations with respect to the solar surface. However, horizontal oscillations both parallel (Gilbert et al. 2008) and perpendicular (Hershaw et al. 2011; Liu et al. 2012b) to the filament axis have also been reported. Hershaw et al. (2011) studied two trains of large-amplitude oscillations in an arched EUV prominence, triggered by coronal waves coming from two successive flares in the same remote active region. The growth of the velocity amplitude with height and the in-phase starting motion of the two legs suggests that the oscillatory behavior is caused by a global kink mode. But the differences in oscillatory characteristics measured in the two legs and a height dependence of the period indicate that the prominence oscillates as a collection of separate but interacting threads. Liu et al. (2012b), on the other hand, reported a coherent oscillation of three different filament threads with approximately the same period, damping time, and initial amplitude, as a fast EUV wave propagates through a cavity in which the filament is embedded, suggestive of the bodily oscillation of the entire cavity.

Here we revisit the renowned X9 flare on 1990 May 24 but concentrate on a Moreton wave and its interactions with filaments, which have not been studied in detail. Although they have been known for decades, observations of Moreton waves are rare, and even more rarely are they captured in such high cadence and spatial resolution as presented in this paper. In the section that follows, we present the analysis and interpretation of the observations. The implications for both the Moreton wave and the filaments are summarized and discussed in Section 3.

2. OBSERVATION AND ANALYSIS

The Hα data used here were originally recorded on 35 mm film at the Big Bear Solar Observatory (BBSO). BBSO's film collection has recently been digitized at NJIT[8] (Liu et al. 2010a; Wang & Liu 2012). The cadence of the film data is usually 1 minute, but during major flares, a flare mode with 10 s cadence is invoked. The digitization was carried out using a commercial film digitizer, which produced 12 bit digital data with a size of 2048×1600 pixels. As a result, the digitized full-disk Hα images obtained by the BBSO 8 inch telescope (with an Airy limit of $0\farcs81$) have a pixel size of $\sim 1\farcs3$, while the partial-disk Hα images obtained by the BBSO 10 inch telescope (with an Airy limit of $0\farcs65$) have a pixel size of $\sim 0\farcs2$. The partial-disk images are capable of offering sub-arcsecond resolution with the excellent seeing conditions at BBSO. The 12 bit images are eventually converted to 8 bit to be displayed on a computer screen, utilizing the nonlinear intensity response of the film reconstructed by the digitizer. A small quiet Sun region at the disk center is used as the reference to align the full-disk images and to remove the intensity variation due to seeing. The limb darkening effect is further removed with a Fourier technique

developed by A. McAllister (see `rm_darklimb` in SolarSoft[9]) when necessary.

The Moreton wave studied here was associated with an X9/1B flare (N33W78) at about 20:48 UT on 1990 May 24 in the NOAA active region 6063. NOAA 6063 is a super-active region with a flare index of 23.5 (Chen et al. 2011). Besides the X9/1B flare on May 24, it also produced an X5/2B flare (N35W36) on May 21. Its prolific flare production is probably due to the complex δ configuration (see NOAA Event Reports). The X5/2B flare was also associated with a Moreton wave that triggered similar filament responses as the May 24 wave. The May 21 event was recorded at one minute cadence on the Sac Peak flare patrol (Smith 1961) films owned by the National Solar Observatory, but the seeing on that day was poor, and BBSO had no observation during the flare time. Hence, we concentrate on the May 24 event in this paper.

Besides prominent microwave (Lee et al. 1994) and hard X-ray (HXR; Pelaez et al. 1992) emission, this renowned X9/1B flare simultaneously produced energetic neutrons, protons, and γ-rays, and has since been studied extensively (Shea et al. 1991; Debrunner et al. 1992, 1993, 1997; Kocharov et al. 1994, 1996; Torsti et al. 1996; Vilmer et al. 2003). The γ-ray lightcurve up to 95 MeV measured by the PHEBUS detector on the *GRANAT* spacecraft shows two peaks at 20:48:12 and 20:48:36 UT, respectively (Debrunner et al. 1997). The first peak coincided with the microwave peak at 20:48:07 UT as observed by the Solar Arrays at the Owens Valley Radio Observatory (Lee et al. 1994). It is impossible to determine the HXR peak due to the saturation of the Gamma camera (up to 572 keV) on board *GRANAT* (Pelaez et al. 1992). A large increase of neutrons greater than 200 MeV was recorded by ground-level neutron monitors starting at 20:49 UT (Shea et al. 1991). The Moreton wave was also briefly described in Kocharov et al. (1994). This paper provides a detailed study of the wave propagation and its interaction with filaments.

2.1. Wave Onset and Propagation

The X9 flare started at 20:46 UT and peaked at 20:49 UT in *GOES* 1–8 Å. From 20:48:28 to 20:48:58 UT, sequential chromospheric brightenings (Balasubramaniam et al. 2005) were observed to "propagate" westward within a narrow corridor (Figure 1(a), see also the accompanying animation). These were network points (marked by arrows) that suddenly brightened ahead of the Moreton wavefront (marked by "+" symbols). In Figure 1(a), four filaments of interest are labeled F1–F4, respectively. Although other filaments in the more remote area were also disturbed by the Moreton wave, we concentrate on these four to study their reaction to the wave passage, because one can clearly see the wavefront sweeping through them. At 20:48:58 UT, the wavefront was half-way across F4 (Figure 1(a)); At 20:50:18 UT (Figures 1(c) and (f)), the wavefront had swept through F2 and F3. F2 remained intact while F3 was disturbed, so did another small filament to the southwest of F3. At 20:51:38 UT (Figures 1(g) and (j)), the wavefront passed through NOAA 6074 and resulted in two flare-like ribbons (marked by a white arrow). From 20:52:18 to 20:53:58 UT, the wavefront swept through F1, which appeared bright sequentially from west to east in difference images (Figures 1(k) and (l)),

To show how the Moreton wave was initiated, we examine the partial-disk images ($\sim 0\farcs2$ pixel^{-1}; $\lesssim 10$ s cadence) obtained by the BBSO 10 inch telescope. Right after the onset of

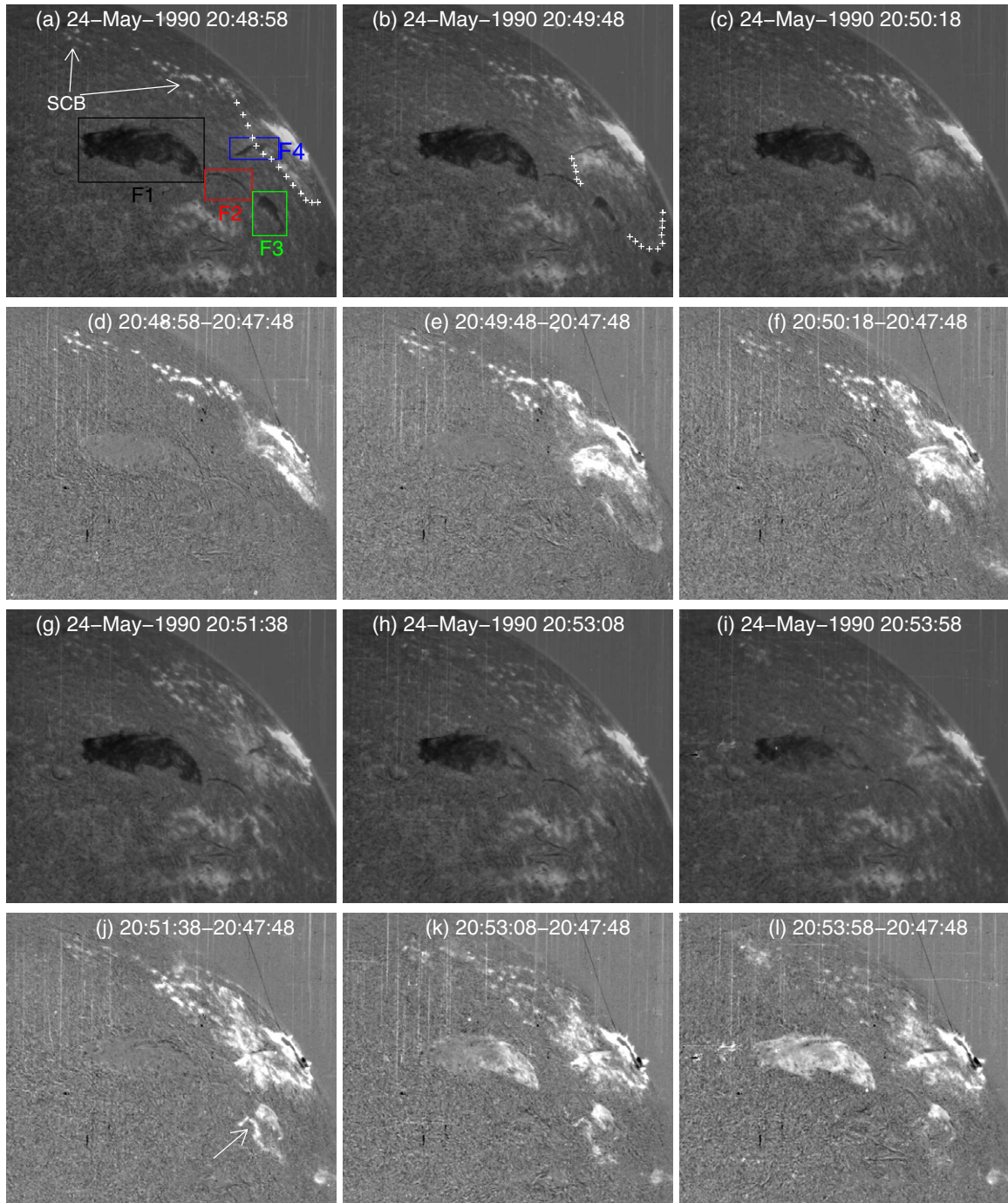**Figure 1.** Sequence of Hα images showing the propagation of the Moreton wave and its interaction with the remote filaments. The initial wavefront is marked by "+" symbols. The colored rectangular boxes enclose the four filaments of interest. The second and fourth rows show corresponding base-difference images.

(An animation and a color version of this figure are available in the online journal.)

the flare, two flare ribbons developed with an indication of a point-symmetric J-shape (Figures 2(a) and (b)), which are interpreted as footpoints of quasi-separatrix layers during the reconnections in the vertical flare current sheet (e.g., Schrijver et al. 2011; Liu et al. 2012a). As the flare progressed, the double J-shaped ribbons expanded into a dumbbell-shaped brightening. Meanwhile, two arc-shaped ribbons (indicated by "×" symbols in Figure 2(c)) appeared in the periphery of the dumbbell-shaped flare brightening. It can be seen that these two arcs were largely stationary if one places the visually picked points ("×" symbols) along the two arcs at 20:48:09 UT over the image taken at

20:48:17 UT (Figure 2(g)). The resulting overall S-shape of the ribbons corresponds well to the structure of separatrixes in a flux rope eruption (Titov 2007). At this moment, the first clear wavefront (marked by "+" symbols) can be recognized, being well separated from the flare brightening. The wavefront soon became diffused and irregular when propagating outward (Figures 2(h) and (i)). At 20:48:57 UT (Figure 2(i)), the Moreton wave was already half sweeping through F4, and the wavefront obviously bulged around the filament region.

At 20:48:09 UT, an intensity enhancement was also observed between the two arcs, as shown in the difference image
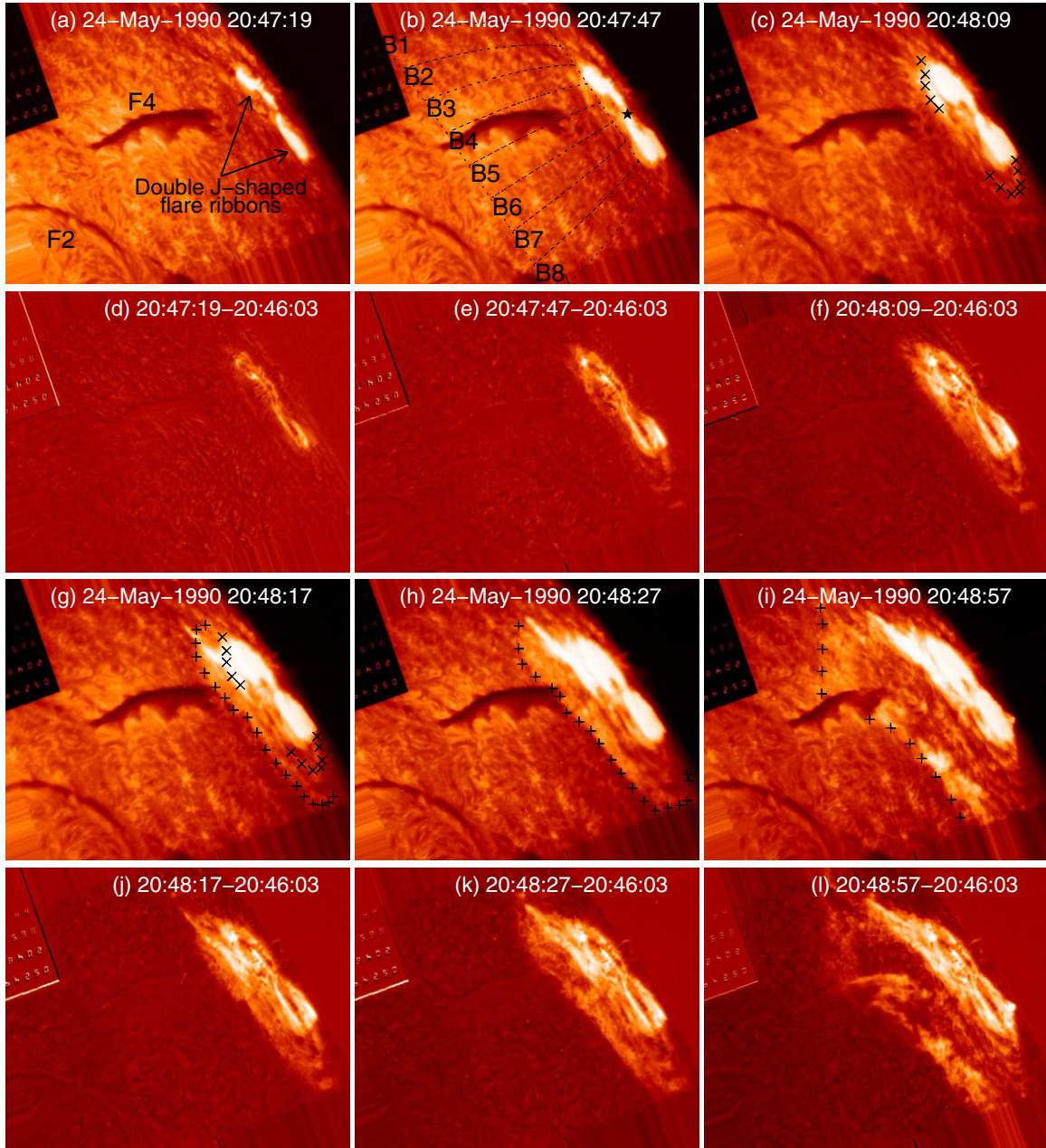
Figure 2. Onset of the Moreton wave observed in high-resolution, high-cadence Hα images obtained by the BBSO 10 inch telescope. Panel (a) shows the angular sectors, B1–B8, used to track the wave propagation. The star symbol indicates the center of the sectors. In the rest of the figure, "×" symbols mark the visually picked points along the arc-shaped ribbons in the periphery of the dumbbell-shaped flaring brightening, while "+" symbols mark the Moreton wavefront.

(An animation and a color version of this figure are available in the online journal.)

(Figure 2(f)). It is possible that the shock front was spatially coincident with the two arcs at that moment. Hence, we put the shock starting time between 20:48:09 and 20:48:17 UT in a conservative manner, which is indicated in the top panel of Figure 3 by a vertical bar. However, due to the difficulty in separating the propagating Moreton wave from the expanding flaring region, the wave could have started earlier.

The top panel of Figure 3 also shows the *GOES* 1–8 Å flux (purple dotted line) and its time derivative (purple solid line), the latter of which, peaking between 20:48:36 and 20:48:39 UT, is generally a good proxy for HXRs (Neupert 1968). It is interesting that the shock starting time coincides with the peak (20:48:07 UT) of the microwave emission (Lee et al. 1994) as well as the first peak (20:48:12 UT) of γ-rays (Debrunner

et al. 1997), although slightly earlier than the peak of the HXR proxy.

We note that Kocharov et al. (1994, page 154) "found that the shock propagation becomes apparent to the eye after 20:47:50 UT." We suspect that they may have identified the stationary arcs (Figures 1(b) and (c)) as the shock front. The arcs developed after 20:47:47 UT but were clearly separated from the shock front at 20:48:17 UT (Figure 1(g)). Assuming that the shock propagates at a uniform speed of ∼1600 km s⁻¹, Kocharov et al. (1994) were also able to pinpoint the shock starting time at 20:47:40 UT by back extrapolation. This may actually be the earliest possible shock starting time, as 1600 km s⁻¹ is close to the lower limit (∼1500 km s⁻¹) of our measurements (see below).
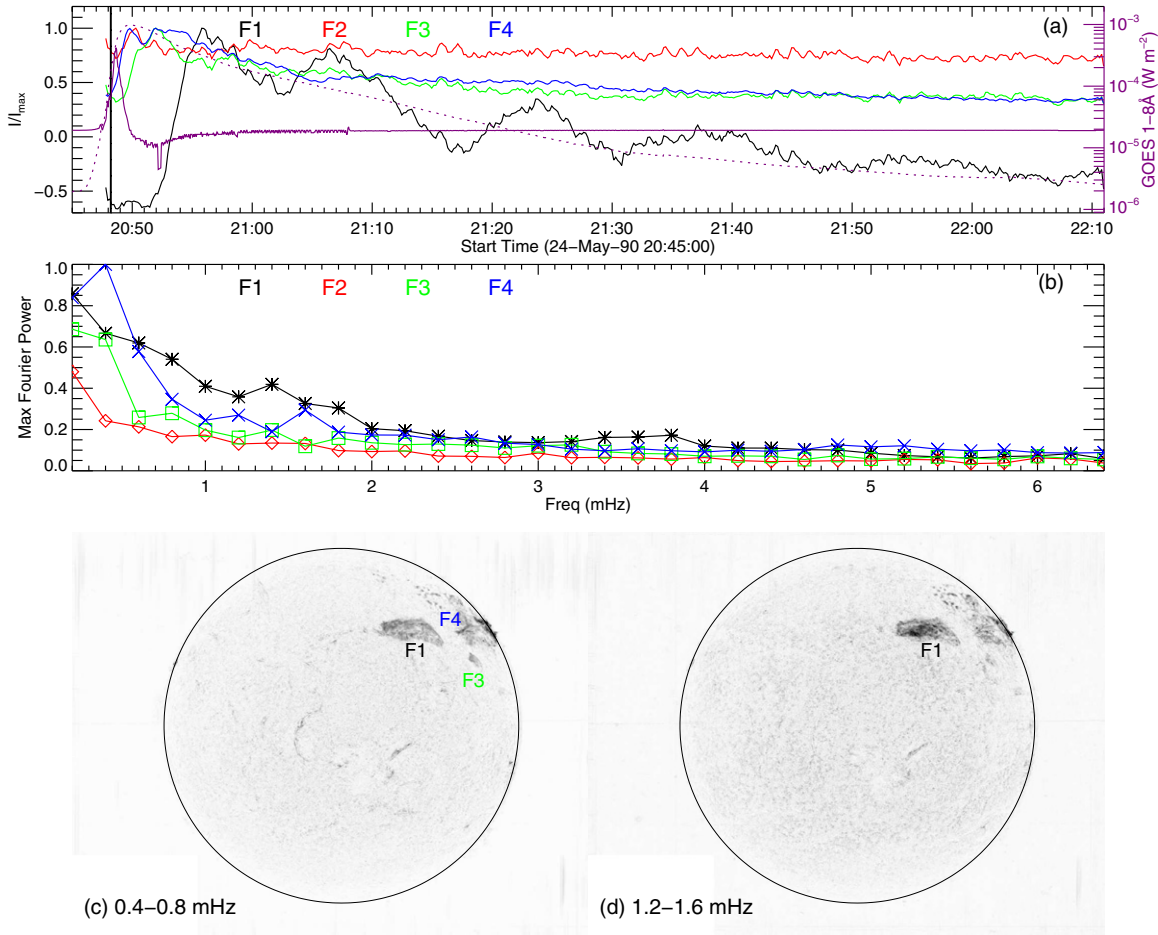
Figure 3. Filament oscillation driven by the Moreton wave. (a) Lightcurves of the filaments F1–F4, color-coded according to the colors of the rectangular boxes in Figure 1(a). The curves are normalized by each own maximum and scaled by the y-axis on the left. Over-plotted are the *GOES* 1–8 Å flux (purple dotted line), scaled by the y-axis on the right, and its time derivative (purple solid line), shown in an arbitrary scale. (b) Maximum Fourier power obtained from each individual rectangular box in Figure 1(a). (c) and (d) Fourier power integrated over relevant frequencies around which the curves in (b) have local maxima. The colors are reversed so that enhanced features appear dark. The solar limb is indicated by the circle.

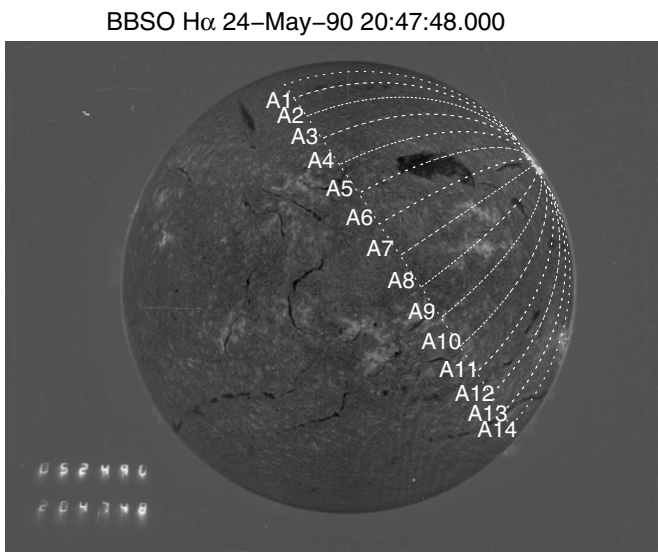(A color version of this figure is available in the online journal.)

Figure 4. Angular sectors, A1–A14, used to the track the wave propagation.

To track the wave propagation, we use a set of 10° wide angular sectors, A1–A14 (Figure 4), centered at the middle of the double J-shaped flare ribbons (785″, 517″), as marked by a star symbol in Figure 2(b). For each sector, we compose base

difference space–time plots by integrating along the azimuthal direction of each sector (Figure 5). The slope of the bright tracks on these plots then indicates the wave propagation speed, which varies from 1600 km s^{-1} to 2600 km s^{-1}. Most tracks lasted for less than five minutes, which signifies the importance of high-cadence observations. We also apply a set of 3° wide sectors, B1–B8 (centered on the same point), to the partial-disk images obtained by the BBSO 10 inch telescope (Figure 2(b)). In the resultant space–time plots of Sectors B1, B2, B4 and B6 (Figure 6), one can clearly see that a fainter, diffuse front deviates from the sharp wavefront. The speed of the first, sharp wavefront ranges from 1500 km s^{-1} to 2600 km s^{-1}, similar to the result obtained from the full-disk observation, whereas the fainter front propagated at much slower speeds of 300–600 km s^{-1}. It can also be seen that the Moreton wave propagated fastest in the sector enclosing F4 (Sector B4), consistent with the fact that the wavefront bulged at this filament (Figure 2(i)).

2.2. Filament Oscillation

We study the response of filaments to the passing Moreton wave by integrating over the rectangular regions in Figure 1(a), enclosing the four filaments F1–F4. Figure 3(a) shows the resultant "lightcurves," which are smoothed by a five-point
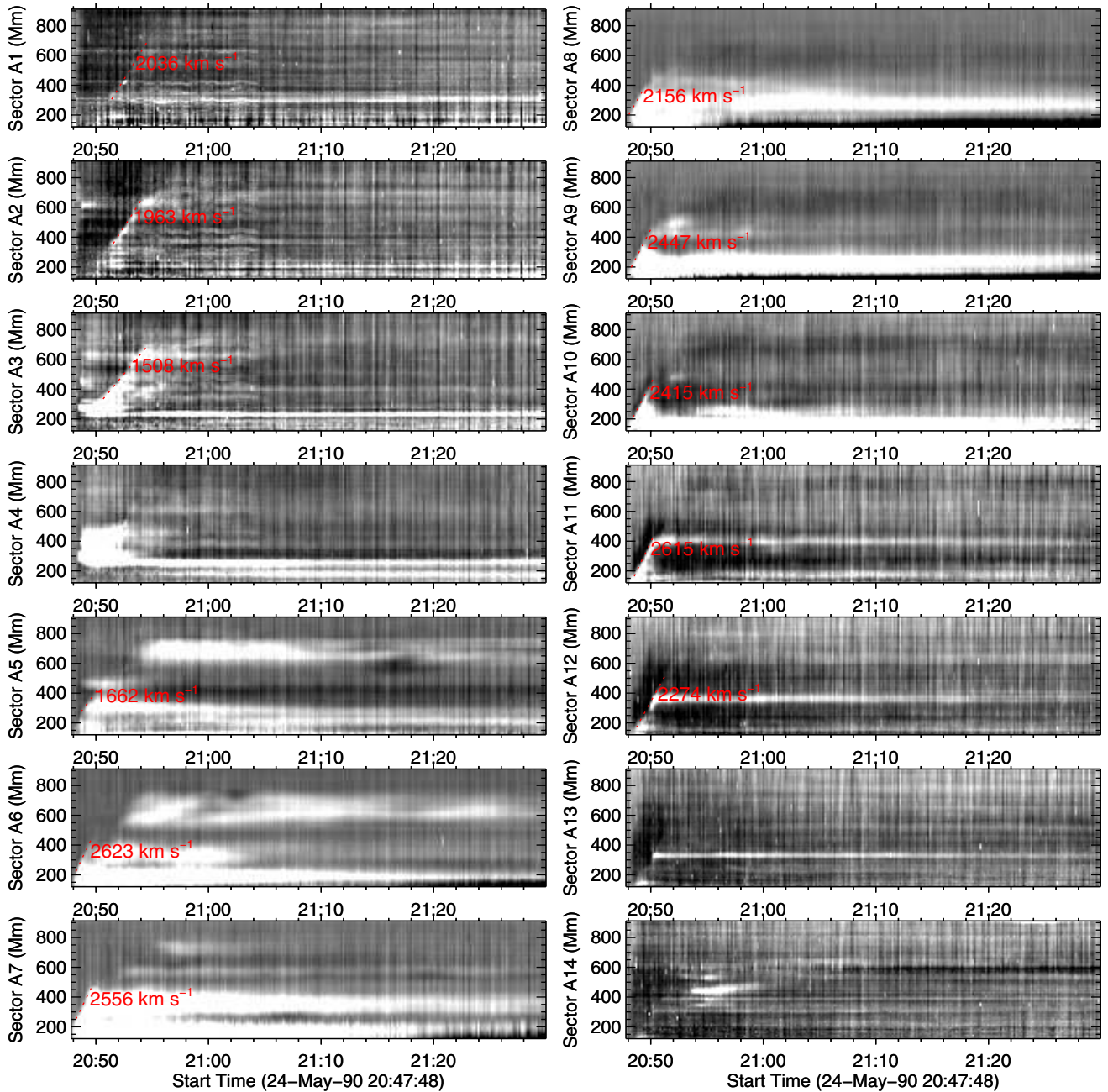
Figure 5. Space–time plots showing the propagation of the Moreton wave as observed by the BBSO 8 inch telescope. The plots are obtained by integrating across each individual sector in Figure 4 along the azimuthal direction and subtracting the initial profile (see the text). The dotted lines show linear fits of visually picked points along the tracks left by the wavefront. The slope of each track indicates the speed of the wavefront.

(A color version of this figure is available in the online journal.)

running box, normalized by their individual maximum, and displayed in the same color as the corresponding rectangular boxes. One can see that F4 (blue), F3 (green), and F1 (black) became bright successively as they were swept by the Moreton wave one after another between 20:50 and 21:00 UT. F3 and F4 then gradually recovered to its initial state by 21:30, whereas F1 quickly reformed (corresponding to dips of the lightcurve) and then partially disappeared (corresponding to peaks of the lightcurve) at least three times after the initial activation. In contrast, F2 (red) changed little when swept by the Moreton wave at approximately the same time as F3 (see also the animation accompanying Figure 2).

We apply Fourier transform to a data cube of 500 images with 10 s cadence from 20:47:48 to 22:10:58 UT, taken from

the full-disk observations by the BBSO 8 inch telescope, which results in a data cube of Fourier maps at various frequencies from 0.2 mHz, as prescribed by the time duration considered, to 0.2 Hz, which is the Nyquist frequency as prescribed by the sampling rate. We then plot in Figure 3(b) the maximum Fourier power versus frequency within the rectangular regions defined in Figure 1(a). One can see that both curves of F3 (green) and F4 (blue) show a bump at about 0.4 mHz, while F1's curve (black) has a plateau at 0.4–0.8 mHz and a bump at 1.4 mHz. In contrast, F2's curve (red) displays no similar features except the DC component. We show in Figures 3(c) and (d) the Fourier power integrated over the relevant frequencies, i.e., 0.4–0.8 mHz and 1.2–1.6 mHz. One can see that in both maps, F1 is shown as an enhanced feature with the same morphology as in the Hα
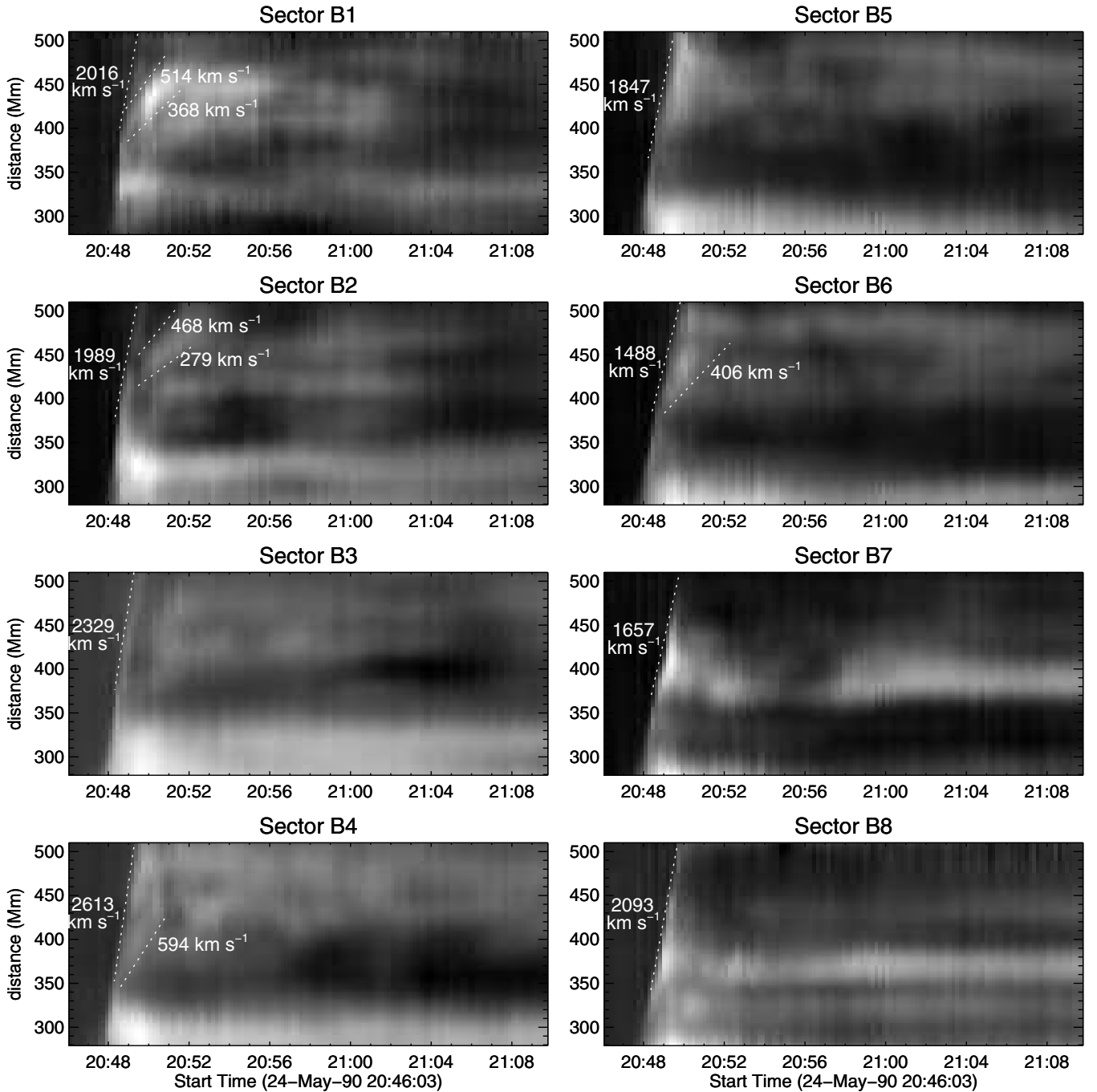
Figure 6. Space–time plots showing the propagation of the Moreton wave as observed by the BBSO 10 inch telescope. The plots are obtained by integrating across each individual sector in Figure 2(a) along the azimuthal direction and subtracting the initial profile (see the text). The dotted lines show linear fits of visually picked points along the tracks left by the fast wavefront as well as a slow, diffuse front.

images. Although F3 and F4 are also enhanced in the Fourier map from 0.4–0.8 mHz, they are not clearly visible in the Fourier map from 1.2–1.6 mHz. Naturally, no sign of F2 can be found in either Fourier map. Thus, the Fourier map at lower frequencies features the filaments disturbed by the Moreton wave, while the map at higher frequencies features the filaments undergoing oscillations.

As F1 shows a prominent oscillatory behavior, we extract the rectangular region enclosing F1, de-stretch the images, and again apply the Fourier transform to this new data cube. Figure 7 shows both the Fourier power and phase at 0.6 mHz and 1.2 mHz. It is remarkable that at 1.2 mHz, most of the fila-

ment region is characterized by similar phases, suggesting that the filament oscillated as a whole. We further look into details of F1's oscillatory behavior by placing a series of slits with a width of 10 pixels (∼10 Mm) in the north–south and east–west directions across F1 (top panel of Figure 7), summing the intensities along the slit width, and generating a series of stack plots (Figures 8 and 9) after further subtracting the initial profile from the first image. Signatures of oscillations are hard to discern in the stack plots made from the E–W slits (Figure 8). It is remarkable, however, that an inclined dark feature can be seen in quite a few stack plots in Figure 8, which resulted from a successive disappearance of the filament material when the
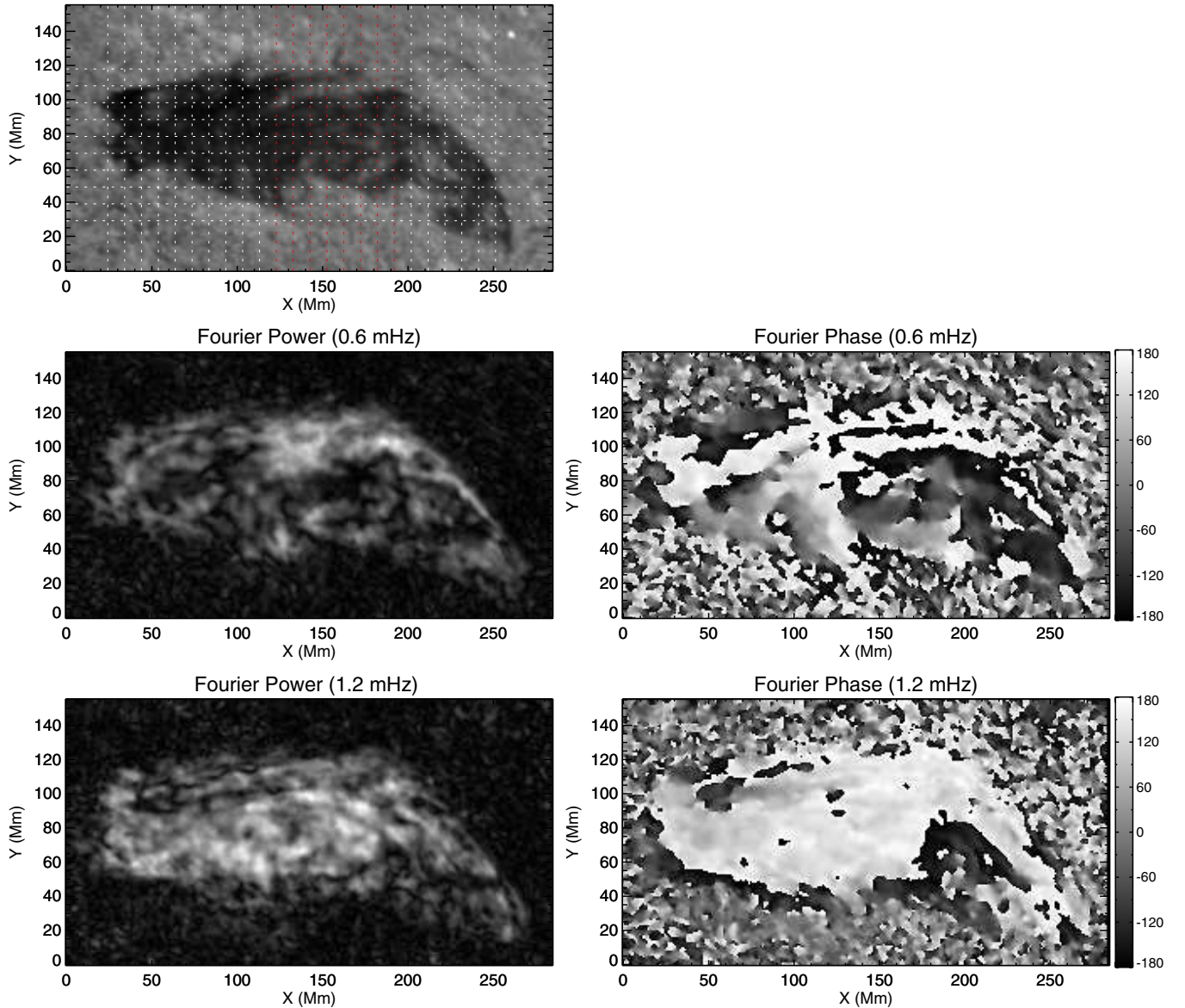
Figure 7. Oscillation of the filament F1. Top: dotted lines indicate the central positions of the slits used in Figures 8 and 9. The lines in red show the central positions of the slits along which the filament material oscillated coherently. The middle and bottom panels show the Fourier power (left) and phase (right; ranging from $-\pi$ to π) at 0.6 and 1.2 mHz, respectively.

(An animation and a color version of this figure are available in the online journal.)

Moreton wave passed through the filament. This feature therefore reflects the speed of the wave propagation, which one can read from its slope, i.e., $\sim$550 km s^{-1}. This is obtained from the stack plot generated with the E–W slit at $Y = 68.6$ Mm, in which the inclined feature is most clear. In the stack plots made from the N–S slits (Figure 9), one can clearly see cosine-like wave patterns for slits whose central positions range from $X = 123$ Mm to $X = 192$ Mm (marked in red in the top panel of Figure 7). Figure 10 shows an exemplary oscillatory pattern, which is reasonably well fitted with a damped cosine function, $A \cos{(2\pi f t + \phi)} \exp{(-t/\tau)}$. The troughs and crests of these wave patterns took place at approximately the same time, which is consistent with the Fourier transform result (Figure 7) signifying that F1 oscillated as a whole. The time duration between two consecutive peaks, i.e., the oscillation period, is about 30 minutes (0.6 mHz in frequency). A difference to note is that in the Fourier analysis it is the second harmonic, i.e., 1.2 mHz, that displays the most prominent coherent Fourier phases.

3. SUMMARY AND DISCUSSION

We investigate the Moreton wave on 1990 May 24 with digitized BBSO Hα film data at excellent temporal cadence ($\lesssim$10 s) and spatial resolution ($\lesssim$1″). The first clear Moreton wavefront appeared at the periphery of the flaring region between 20:48:09 and 20:48:17 UT, which is slightly earlier (about 20–30 s) than the peak of the soft X-ray flux time derivative, but coincides with both the microwave peak and the first of the two γ-rays peaks. This might be a manifestation of the so called "Big Flare Syndrome" (Kahler 1982). The wavefront initially propagated at $\sim$2000 km s^{-1}, followed by a slower diffuse front at 300–600 km s^{-1} about 1 minute after the wave onset. To our knowledge, this slow front is detected in Hα for the first time. Asai et al. (2012) also reported that a fast EUV wavefront precedes a slow EUV front, with the surface part of the fast front co-spatial with an Hα Moreton wave. Recent *STEREO* and *Solar Dynamics Observatory* observations
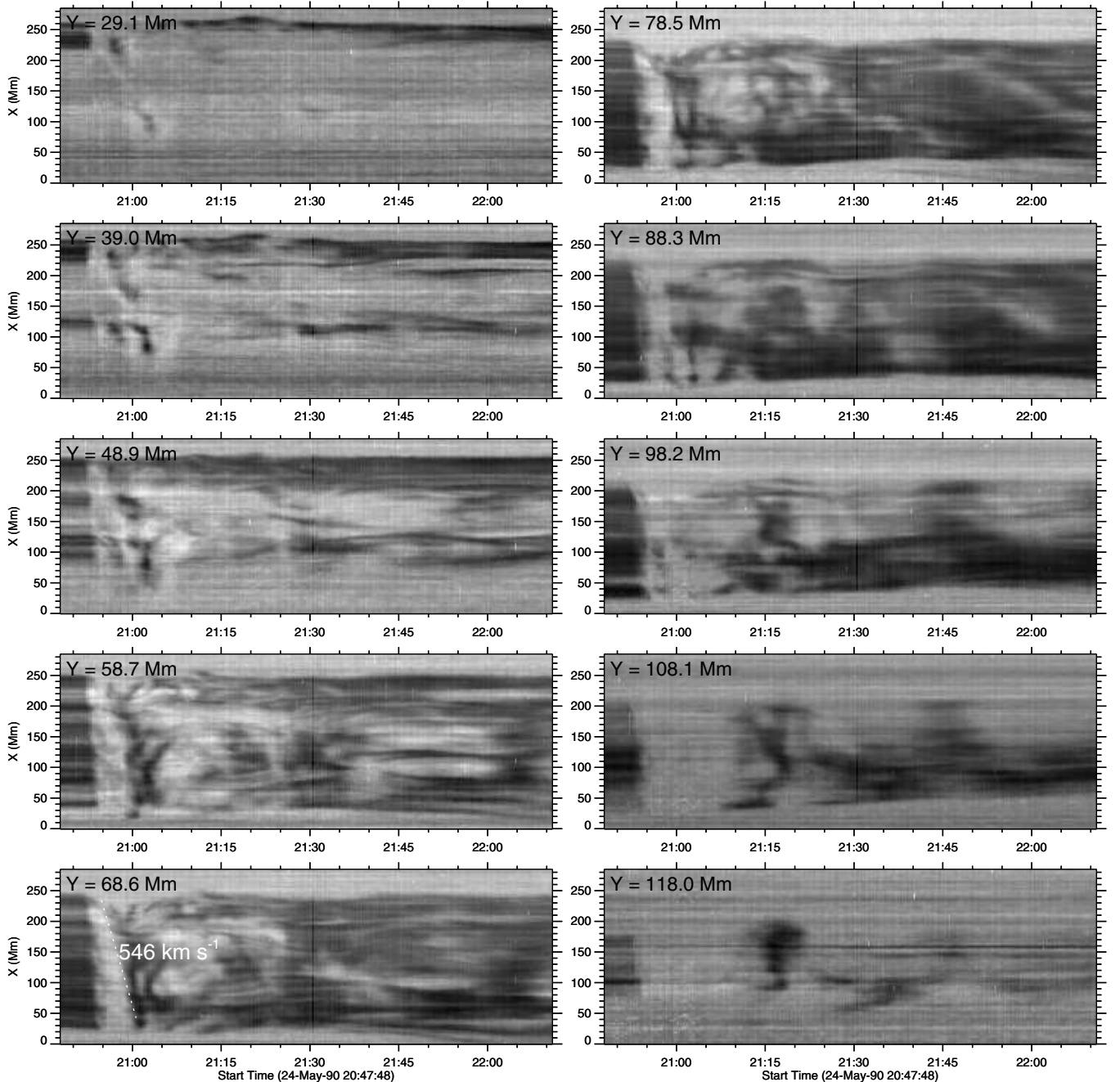
Figure 8. Evolution of F1 seen though the east–west oriented slits in the top panel of Figure 7. In the stack plot obtained with the horizontal slit at $Y = 68.6$ Mm, the dotted line shows a linear fit to visually picked points along an inclined dark feature.

often show that the CME and the EUV wave are initially cospatial and then quickly decouple with the deceleration of the CME's lateral expansion (Patsourakos & Vourlidas 2009, 2012; Kienreich et al. 2009; Liu et al. 2010b, 2012b; Chen & Wu 2011; Cheng et al. 2012), which has also been demonstrated in three-dimensional (3D) MHD simulations (Cohen et al. 2009; Downs et al. 2012). However, in the absence of coronal observations, we could only speculate that the wavefronts observed in this study should have a close spatio-temporal relationship with the disturbances propagating in the corona. It is unclear whether the slow, diffuse front corresponds to a real MHD wave, or to the CME-caused coronal restructuring. The Moreton wave decelerated to ∼550 km s^{-1} as it swept through the filament F1 at about 21:00 UT, suggesting that at that time the Moreton

wave was probably freely propagating as a decelerating blast wave. The average deceleration is about 2 km s^{-2}, comparable to previous results on large-scale waves (Warmuth et al. 2004a, 2004b).

The wave–filament interaction yields insights into physical properties of both the wave and the filaments (e.g., Gilbert et al. 2008), which can be summarized as follows. (1) The coronal nature of the wave phenomenon which is seen in the chromosphere as a Moreton wave and the different filament properties together may result in the distinct response of F1–F4 to the passing wave. (2) The forward inclination of the wavefront and the enhancement of the local Alfvén speed at the filament channel together can account for the bulge of the wavefront when propagating along the spine of F4. (3) The oscillation of
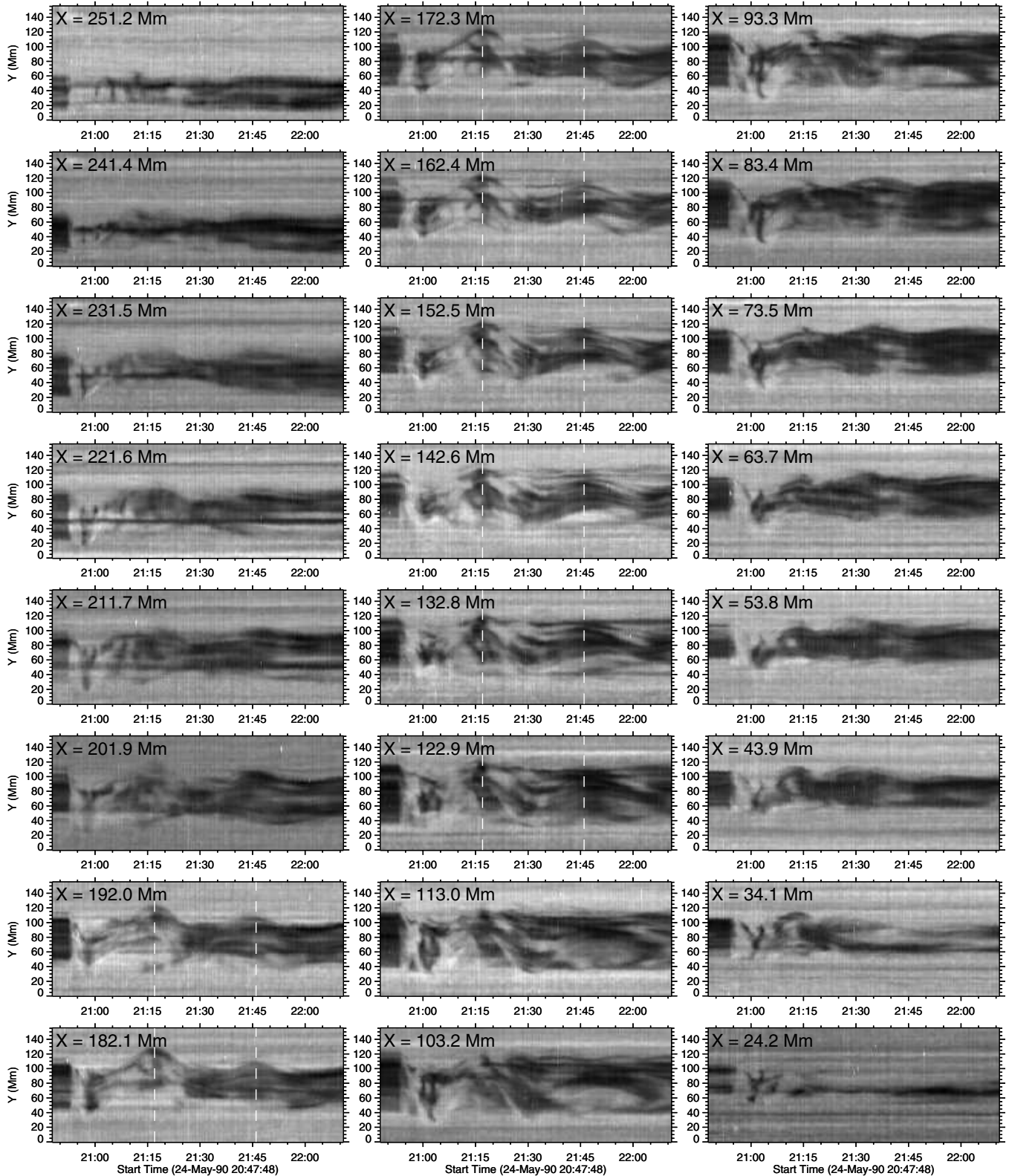
Figure 9. Evolution of F1 seen though the north–south oriented slits in the top panel of Figure 7. The dashed lines mark the peaks of a sine-like pattern.

F1 is primarily perpendicular to the filament spine, suggesting that the oscillation is dominated by a fast kink mode. (4) The coherent Fourier phases across F1 indicates that the magnetic system supporting the filament oscillates as a whole and that this wave–filament interaction can be modeled as a driven harmonic oscillator. (5) F1's oscillation is featured by ~1 mHz signals.

Jackiewicz & Balasubramaniam ([2013]) obtained a similar frequency for filaments disturbed by the 2006 December 6 Moreton wave, but with a much smaller velocity amplitude (<1 km s^{-1}). Whether or not this is a characteristic frequency of filaments is worthy of further investigation. (6) The lack of eruption of the wave-swept filaments signifies the stability
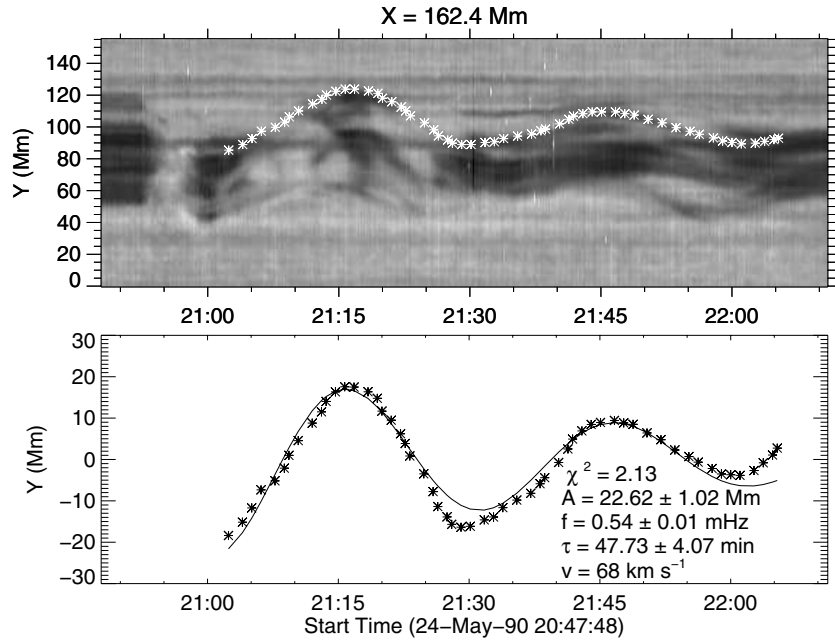
Figure 10. Oscillatory pattern fitted with a damped cosine function. The top panel shows the space–time evolution as seen through the N–S slit at $X = 162.4$ Mm (Figure 9). Visually picked points featuring the oscillatory pattern are indicated by white asterisks. After de-trended with a second-order polynomial, these points are fitted with a damped cosine function, i.e., $A \cos(2\pi f t + \phi) \exp(-t/\tau)$. The fitting results are given in the bottom panel. The velocity amplitude is obtained from the derivative of the damped cosine function.

of the filament magnetic system. (4)–(6) may provide important constraints to filament models. Remarks (1)–(3) are further detailed below.

We speculate that the distinct responses of the wave-swept filaments pertain to the coronal nature of the Moreton wave (Balasubramaniam et al. 2007). Of the four filaments studied here, only the thickest filament (F1) oscillated, the thinnest filament F2 did not move at all, and the other two filaments (F3 and F4) of medium thickness were activated and then gradually recovered. The apparent thickness of a filament can be attributed partially to its vertical extension in projection. This is obvious for F1. Figure 11 shows the evolution of the four filaments of interest during 1990 May 21–24. It is noteworthy that F1 became thicker and thicker during its disk passage. On 1990 May 24, it blocked the view of the filament segment to the northeast of F2. With a stereoscopic method (see the Appendix), we estimate that the maximum heights of F1–F4 are 63, 25, 46, and 38 Mm, respectively. This suggests that oscillations are triggered by the wave only if the filaments reach above a certain height. This height must exceed 25 Mm (F2's height), but be comparable to F3 and F4's heights. As a comparison, Patsourakos et al. (2009) derived an EUV wavefront height of about 90 Mm with *STEREO* data. On the other hand, one can see from Figure 11 that F2, F3, and F4 are located in the same filament channel aligned along a curved polarity inversion line. Hence, F3 and F4 may be embedded in a similar magnetic environment, even though they are quite separated, which could explain why they behave similarly to the passing Moreton wave. Their gradual recovery following the activation implies much stronger damping than what F1 experienced. Whether or not this is related to their magnetic configuration remains to be investigated.

The cause of the wavefront bulging at F4 (Figure 2) could be twofold. On the one hand, this might be a manifestation of a forwardly inclined wavefront toward the surface (Vršnak et al. 2002; Warmuth et al. 2004b; Gilbert et al. 2008; Liu et al. 2012b). In other words, it is the wavefront higher up

in the corona that appears as the bulge at the filament, which is essentially a coronal structure. One the other hand, the bulged wavefront may reflect the enhanced Alfvén speed in the filament channel. Filament channels are known to be the disk counterpart of prominence cavities observed above the limb, which are characterized by higher magnetic field strength and lower plasma density than the surrounding corona (Leroy 1989; Gibson et al. 2006). Liu et al. (2012b) reported a fast EUV wave propagating through a cavity with an embedded filament at 50% faster speeds than outside, suggesting that the wave propagates at the local fast-mode velocity. Moreton waves are known to avoid regions of enhanced Alfvén speeds, such as active regions and coronal holes (e.g., Liu et al. 2006; Balasubramaniam et al. 2007). Similar behaviors are observed for global EUV waves (e.g., Gopalswamy et al. 2009; Li et al. 2012). Theoretical studies have also demonstrated that the ray trajectory of an MHD wave would be deflected away from regions of high wave speeds toward those of low wave speeds (Uchida 1968; Wang 2000; Afanasyev & Uralov 2011). Thus, the bulged Moreton wavefront is a reflection of its wave nature.

The filament material within F1 oscillated primarily perpendicular to the filament axis, which is demonstrated through its "winking" in the Hα center (the line-of-sight component), and in the oscillatory patterns seen through the north–south oriented slits (the plane-of-sky component). If we consider the probability that the horizontal oscillation is derived from the plane-of-sky projection of a purely vertical oscillation as a result of the enhanced pressure behind the (large-amplitude or shocked) wavefront pushing down the chromosphere, then we may estimate the velocity amplitude of the vertical oscillation because $v_{\parallel} = v_{\perp} \sin \theta$, where $\theta \simeq 30°$ is the latitude of F1 and $v_{\parallel} \simeq 69$ km s^{-1} is obtained from the fitting result (Figure 10). This gives $v_{\perp} \simeq 138$ km s^{-1}. Similarly, the displacement amplitude of the vertical oscillation is estimated to be as large as 44.5 Mm. The vertical oscillation must have a significant component perpendicular to the filament's magnetic field, which is known to
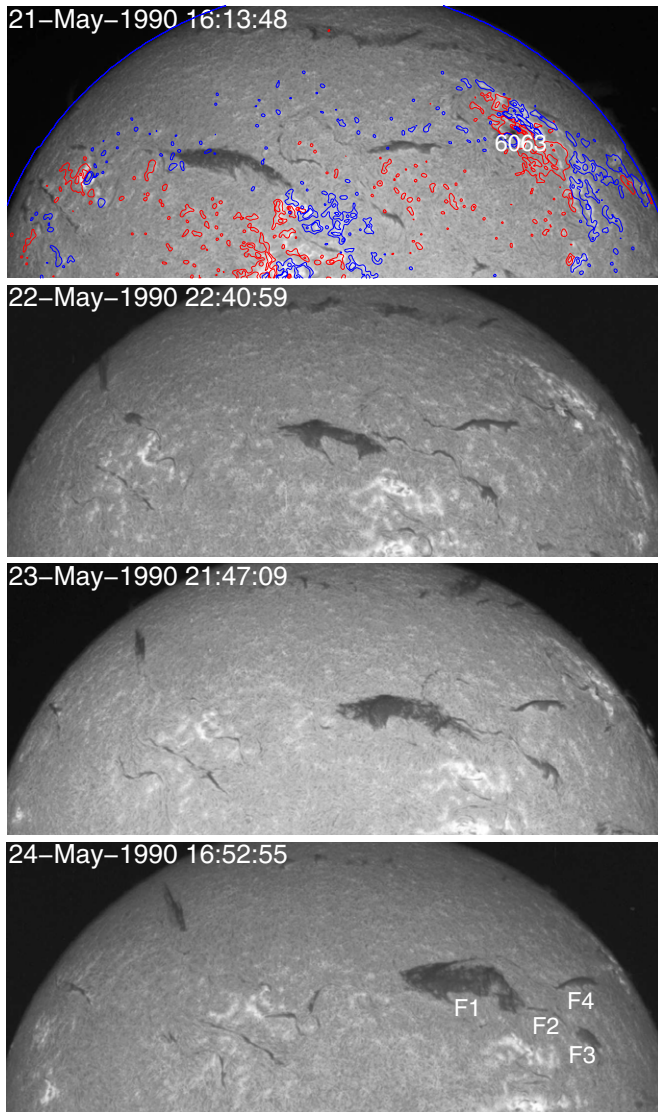
Figure 11. Evolution of the filaments of interest from 1990 May 21 till 24, prior to the initiation of the Moreton wave. The top panel is overlaid by a magnetogram taken at approximately the same time at Kitt Peak by National Solar Observatory. The contours show the line-of-sight component of the photospheric field at levels of ±200, ±50 G, with red (blue) colors indicating positive (negative) polarities.
(A color version of this figure is available in the online journal.)

Table 1
Three-dimensional Reconstruction of Filament Heights

Filament	Num_p[a]	Length[b] (Mm)	h_{max}[c] (Mm)	Err[d] (Mm)
F1	7	247.0	63.5	3.7
F2	4	48.3	25.2	2.5
F3	5	46.4	46.5	2.4
F4	9	108.9	38.8	7.8

Notes.
[a] Number of tiepoints.
[b] Length from the first tiepoint to the last along the filament spine.
[c] Maximum height among the tiepoints.
[d] Three-dimensional reconstruction error associated with the maximum height.

APPENDIX

FILAMENT HEIGHT

The filament height is estimated with the 3D triangulation and reconstruction method developed by Aschwanden et al. (2008). For slowly evolving structures like filaments, the ground-based observations at two different times, say, one day apart, can be utilized to get two separated views for stereoscopy (e.g., Xu et al. 2010). In this practice, the parallax angle between two "observers" results from solar rotation rather than from two satellites like the *STEREO* mission. One caveat is that the Sun rotates at different speeds with latitude, known as differential rotation. Besides, the rotation speed also varies with different heights. We adopt here a synodic rotation rate of 13.3044 ± 0.0003 deg day^{-1} (see Table 2 in Steinegger et al. 2001), which is obtained by measuring the displacements of chromospheric features with a cross-correlation technique.

The data processing following Aschwanden et al. (2008) includes calibration, co-alignment, intensity normalization, feature tracing, coordinate transfer, stereoscopic 3D reconstruction, and curvilinear fitting. The tracing step for filaments, however, is done visually because unlike coronal loops, filaments are much more extended and do not take a simple geometric shape. Basically, the same feature in a pair of images are manually identified, which is referred to as "tiepointing." Here we select only "tiepoints" along the outer edge of the filament spine. Each tiepoint pair is used to find the corresponding point in the 3D heliocentric coordinate system and derive the filament's height (see more details in Xu et al. 2010). Using a pair of Hα images prior to the flare, taken at 21:34:29 UT on 1990 May 23 and at 20:45:48 UT on May 24, we obtain the maximum heights of the filaments F1–F4 as listed in Table 1.

be dominantly horizontal, with the angle between the field vector and the filament axis being 25° on average (Leroy 1989; Bommier et al. 1994). Thus, the excited wave mode in the filament is very likely a fast kink mode.

To conclude, the excellent spatial and temporal resolution of the observation presented here equips us with a better understanding of the physical properties of both filaments and Moreton waves, which are potentially useful as inputs/constraints for models. The Global High Resolution H-alpha Network[10] operated by NJIT has set out to provide regular off-band Hα observations, which will help advance the studies of Moreton waves and wave–filament interactions.

REFERENCES

Afanasyev, A. N., & Uralov, A. M. 2011, SoPh, 273, 479
Arregui, I., Oliver, R., & Ballester, J. L. 2012, LRSP, 9, 2

---

[10] http://swrl.njit.edu/ghn_web/

Asai, A., Ishii, T. T., Isobe, H., et al. 2012, ApJL, 745, L18
Aschwanden, M. J., Wülser, J.-P., Nitta, N. V., & Lemen, J. R. 2008, ApJ, 679, 827
Athay, R. G., & Moreton, G. E. 1961, ApJ, 133, 935
Balasubramaniam, K. S., Cliver, E. W., Pevtsov, A., et al. 2010, ApJ, 723, 587
Balasubramaniam, K. S., Pevtsov, A. A., & Neidig, D. F. 2007, ApJ, 658, 1372
Balasubramaniam, K. S., Pevtsov, A. A., Neidig, D. F., et al. 2005, ApJ, 630, 1160
Bommier, V., Landi Degl'Innocenti, E., Leroy, J.-L., & Sahal-Brechot, S. 1994, SoPh, 154, 231
Chen, A. Q., Wang, J. X., Li, J. W., Feynman, J., & Zhang, J. 2011, A&A, 534, A47
Chen, P. F., Fang, C., & Shibata, K. 2005, ApJ, 622, 1202
Chen, P. F., & Wu, Y. 2011, ApJL, 732, L20
Cheng, X., Zhang, J., Olmedo, O., et al. 2012, ApJL, 745, L5
Cohen, O., Attrill, G. D. R., Manchester, W. B., IV, & Wills-Davey, M. J. 2009, ApJ, 705, 587
Debrunner, H., Lockwood, J. A., Barat, C., et al. 1997, ApJ, 479, 997
Debrunner, H., Lockwood, J. A., & Ryan, J. M. 1992, ApJL, 387, L51
Debrunner, H., Lockwood, J. A., & Ryan, J. M. 1993, ApJ, 409, 822
Dodson, H. W., & Hedeman, E. R. 1964, NASSP, 50, 15
Downs, C., Roussev, I. I., van der Holst, B., Lugaz, N., & Sokolov, I. V. 2012, ApJ, 750, 134
Eto, S., Isobe, H., Narukage, N., et al. 2002, PASJ, 54, 481
Gibson, S. E., Foster, D., Burkepile, J., de Toma, G., & Stanger, A. 2006, ApJ, 641, 590
Gilbert, H. R., Daou, A. G., Young, D., Tripathi, D., & Alexander, D. 2008, ApJ, 685, 629
Gopalswamy, N., Yashiro, S., Temmer, M., et al. 2009, ApJL, 691, L123
Grechnev, V. V., Afanasyev, A. N., Uralov, A. M., et al. 2011, SoPh, 273, 461
Harra, L. K., Sterling, A. C., Gömöry, P., & Veronig, A. 2011, ApJL, 737, L4
Hershaw, J., Foullon, C., Nakariakov, V. M., & Verwichte, E. 2011, A&A, 531, A53
Hudson, H. S., Khan, J. I., Lemen, J. R., Nitta, N. V., & Uchida, Y. 2003, SoPh, 212, 121
Hyder, C. L. 1966, ZA, 63, 78
Jackiewicz, J., & Balasubramaniam, K. S. 2013, ApJ, 765, 15
Kahler, S. W. 1982, JGR, 87, 3439
Kienreich, I. W., Temmer, M., & Veronig, A. M. 2009, ApJL, 703, L118
Kocharov, L., Kovaltsov, G., Torsti, J., et al. 1996, in AIP Conf. Proc. 374, ed. R. Ramaty, N. Mandzhavidze, & X.-M. Hua (Melville, NY: AIP), 246
Kocharov, L. G., Lee, J. W., Zirin, H., et al. 1994, SoPh, 155, 149
Lee, J. W., Gary, D. E., & Zirin, H. 1994, SoPh, 152, 409
Leroy, J. L. 1989, in Dynamics and Structure of Quiescent Solar Prominences, ed. E. R. Priest (Astrophysics and Space Science Library, Vol. 150; Dordrecht: Kluwer), 77
Li, T., Zhang, J., Yang, S., & Liu, W. 2012, ApJ, 746, 13
Liu, C., Deng, N., Liu, R., et al. 2012a, ApJL, 745, L4
Liu, C., Lee, J., Deng, N., Gary, D. E., & Wang, H. 2006, ApJ, 642, 1205
Liu, C., Liu, R., Xu, Y., & Wang, H. 2010a, BAAS, 41, 879
Liu, W., Nitta, N. V., Schrijver, C. J., Title, A. M., & Tarbell, T. D. 2010b, ApJL, 723, L53

Liu, W., Ofman, L., Nitta, N. V., et al. 2012b, ApJ, 753, 52
Moreton, G. E. 1960, AJ, 65, 494
Moreton, G. E., & Ramsey, H. E. 1960, PASP, 72, 357
Muhr, N., Vršnak, B., Temmer, M., Veronig, A. M., & Magdalenić, J. 2010, ApJ, 708, 1639
Neupert, W. M. 1968, ApJL, 153, L59
Okamoto, T. J., Nakai, H., Keiyama, A., et al. 2004, ApJ, 608, 1124
Patsourakos, S., & Vourlidas, A. 2009, ApJL, 700, L182
Patsourakos, S., & Vourlidas, A. 2012, SoPh, 281, 187
Patsourakos, S., Vourlidas, A., Wang, Y. M., Stenborg, G., & Thernisien, A. 2009, SoPh, 259, 49
Pelaez, F., Mandrou, P., Niel, M., et al. 1992, SoPh, 140, 121
Ramsey, H. E., & Smith, S. F. 1966, AJ, 71, 197
Schrijver, C. J., Aulanier, G., Title, A. M., Pariat, E., & Delannée, C. 2011, ApJ, 738, 167
Shea, M. A., Smart, D. F., & Pyle, K. R. 1991, GeoRL, 18, 1655
Shen, Y., & Liu, Y. 2012, ApJL, 752, L23
Smith, H. J. 1961, A Study of Sacramento Peak Flares I: Distribution, Areas and Growth Curves, Air Force Cambridge Research Laboratories Technical Note No. 59 of GRD Research Notes, Office of Aerospace Research, U.S. Air Force
Smith, S. F., & Harvey, K. L. 1971, in Physics of the Solar Corona, ed. C. J. Macris (Astrophysics and Space Science Library, Vol. 27; Dordrecht: Reidel), 156
Steinegger, M., Denker, C., Goode, P. R., et al. 2001, in ESA Special Publication, Vol. 464, Proceedings of the SOHO 10/GONG 2000 Workshop: Helio- and Asteroseismology at the Dawn of the Millennium, ed. A. Wilson & P. L. Pallé (Noordwijk: ESA Publications Division), 315
Temmer, M., Vršnak, B., Žic, T., & Veronig, A. M. 2009, ApJ, 702, 1343
Titov, V. S. 2007, ApJ, 660, 863
Torsti, J., Kocharov, L. G., Vainio, R., Anttila, A., & Kovaltsov, G. A. 1996, SoPh, 166, 135
Tripathi, D., Isobe, H., & Jain, R. 2009, SSRv, 149, 283
Uchida, Y. 1968, SoPh, 4, 30
Veronig, A. M., Gomory, P., Kienreich, I. W., et al. 2011, ApJL, 743, L10
Vilmer, N., MacKinnon, A. L., Trottet, G., & Barat, C. 2003, A&A, 412, 865
Vršnak, B., Warmuth, A., Brajša, R., & Hanslmeier, A. 2002, A&A, 394, 299
Wang, H., & Liu, C. 2012, ApJ, 760, 101
Wang, Y.-M. 2000, ApJL, 543, L89
Warmuth, A. 2007, in The High Energy Solar Corona: Waves, Eruptions, Particles, ed. K.-L. Klein & A. L. MacKinnon (Lecture Notes in Physics, Vol. 725; Berlin: Springer), 107
Warmuth, A., Vršnak, B., Aurass, H., & Hanslmeier, A. 2001, ApJL, 560, L105
Warmuth, A., Vršnak, B., Magdalenić, J., Hanslmeier, A., & Otruba, W. 2004a, A&A, 418, 1101
Warmuth, A., Vršnak, B., Magdalenić, J., Hanslmeier, A., & Otruba, W. 2004b, A&A, 418, 1117
Wills-Davey, M. J., & Attrill, G. D. R. 2009, SSRv, 149, 325
Wu, S. T., Zheng, H., Wang, S., et al. 2001, JGR, 106, 25089
Xu, Y., Jing, J., & Wang, H. 2010, SoPh, 264, 81